Ocean Modelling 185 (2023) 102250

Contents lists available at ScienceDirect

Ocean Modelling

journal homepage: www.elsevier.com/locate/ocemod

Normal and reverse storm surges along the coast of Florida during the September 2022 Hurricane Ian: Observations, analysis, and modelling

Mohammad Heidarzadeh [a,*], Takumu Iwamoto [b], Jadranka Šepić [c], Iyan E. Mulia [d,e]

[a] Department of Architecture and Civil Engineering, University of Bath, Bath BA2 7AY, UK
[b] Tsunami and Storm Surge Group, Port and Airport Research Institute, Yokosuka 239-0826, Japan
[c] University of Split, Faculty of Science, Split, Croatia
[d] Prediction Science Laboratory, RIKEN Cluster for Pioneering Research, 7-1-26 Minatojima-minami-machi, Chuo-ku, Kobe 650-0047, Japan
[e] Disaster Resilience Science Team, RIKEN Center for Advanced Intelligence Project, 1-4-1 Nihonbashi, Chuo-ku, Tokyo 103-0027, Japan

ARTICLE INFO

Keywords:
Caribbean Sea
Florida
Hurricane
Storm surge
Sea level data
Atmosphere
Numerical modelling

ABSTRACT

The September 2022 Hurricane Ian was among the most destructive hurricanes to hit the US coasts. Ian was one of the rare events that produced both positive (normal) and negative (reverse) surges. We analyse and model the generation mechanism of these surges through studying sea level, air pressure, and wind observations as well as numerical modelling. Analysis of a rich observation dataset helped us to explain their simultaneous generations for the first time. Among the examined data, maximum wind speed was 50–60 m/s and the minimum air pressure was 961.6 hPa. Although three factors of wind, pressure drop, and geometry contribute to surge generation, we found that wind was the dominant factor. Despite the opposing impacts of pressure drop and wind on reverse surge generation, the amplitudes of reverse surges (2.4 m) were larger than those of normal surges (over 1.8 m). Normal and reverse surges were consistently generated by landward and seaward winds, respectively. Reverse surges occurred at parts of the coast under seaward wind that experienced less intensive pressure drop. We successfully modelled both normal and reverse surges. Our model can be employed for forecasting unique storm surges such as those generated during Hurricane Ian.

1. Introduction

The September 2022 Hurricane Ian was among the most destructive hurricanes to hit Florida as it made landfall as a Category four (Cat-4) hurricane in the Saffir–Simpson hurricane wind scale (SSHS) (Fig. 1) with wind speed of approximately 240 km/h. This is unlike most hurricanes that normally downgrade to Cat-1 or Cat-2 before making landfall. According to various media reports based on officials, at least 154 deaths were reported in Florida (149 deaths) and North Carolina (5 deaths) as of January 2023 along with a damage estimate of approximately US$ 67 billion. Assuming the current damage estimate for Ian, it ranks fifth in terms of total damage after the 2007 Hurricane Katrina (US$ 125 billion; NHC, 2018; Fritz et al., 2007), 2017 Hurricane Harvey (US$ 125 billion; NHC, 2018; Sebastian et al., 2017), 2017 Hurricane Maria (US$ 91 billion; Heidarzadeh et al., 2018), and 2021 Hurricane Ida (US$ 75 billion; Beven et al., 2022).

The United States National Hurricane Centre (NHC) started tracking Hurricane Ian from 19th September 2022 as a tropical wave (NHC, 2022). On 24th September, the system was given the name Ian as it entered the Caribbean Sea and achieved a wind speed of 65 km/h. Consequently, Ian underwent rapid intensification and made landfall as a Cat −3 hurricane in west Cuba (Fig. 1) on 27th September. Following landfall in Cuba, Ian continued gaining strength and became a Cat −4 major Hurricane with maximum wind speed of approximately 250 km/h. At the point of landfall in southwest of Florida, Ian was a Cat −4 major hurricane with wind speed of nearly 240 km/h. Rapid degradation of Ian was observed after landfall in Florida as it became a Tropical Storm at the eastern coast of Florida (Fig. 1). While located offshore eastern Florida, the system once again intensified until it made landfall as a Cat −1 hurricane along the coast of South Carolina before being reduced to a Tropical Storm again (Fig. 1).

The objective of this research is to study the characteristics of storm surges generated by the September 2022 Hurricane Ian, and to explain the mechanism responsible for the simultaneous generation of normal (or positive) and reverse (or negative) storm surges observed during this event. Normal storm surges are a well-known phenomenon during hurricanes and typhoons and are reported during many events worldwide (e.g., Le et al., 2019; Heidarzadeh et al., 2018, 2021 and Heidarzadeh and Rabinovich, 2021). However, hurricanes also can simultaneously generate reverse storm surges meaning that

* Corresponding author.
E-mail address: mhk58@bath.ac.uk (M. Heidarzadeh).
URL: https://researchportal.bath.ac.uk/en/persons/mohammad-heidarzadeh (M. Heidarzadeh).

https://doi.org/10.1016/j.ocemod.2023.102250
Received 2 May 2023; Received in revised form 26 June 2023; Accepted 20 July 2023
Available online 27 July 2023

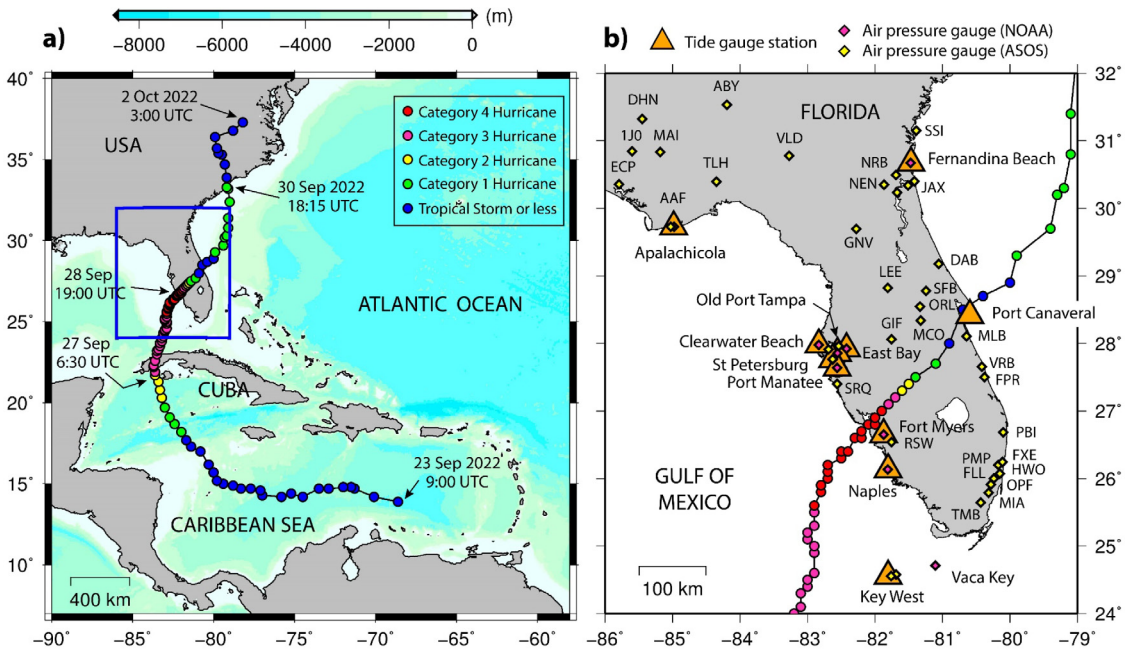

Fig. 1. **(a)** Map showing the track of the September 2022 Category-4 Hurricane Ian and the evolution of its strength along the track. The colour code indicates the strength of the hurricane along the track from Tropical Storm (blue) to Category 4 (red). The blue rectangle shows the area enlarged in the right panel. **(b)** The map of Florida showing the locations of tide gauge (orange triangles) and air pressure (magenta diamonds for NOAA; yellow diamonds for ASOS) stations used in this study. Hurricane track data is from https://www.wunderground.com/. The ASOS station names and their abbreviated codes are provided in Table 1.

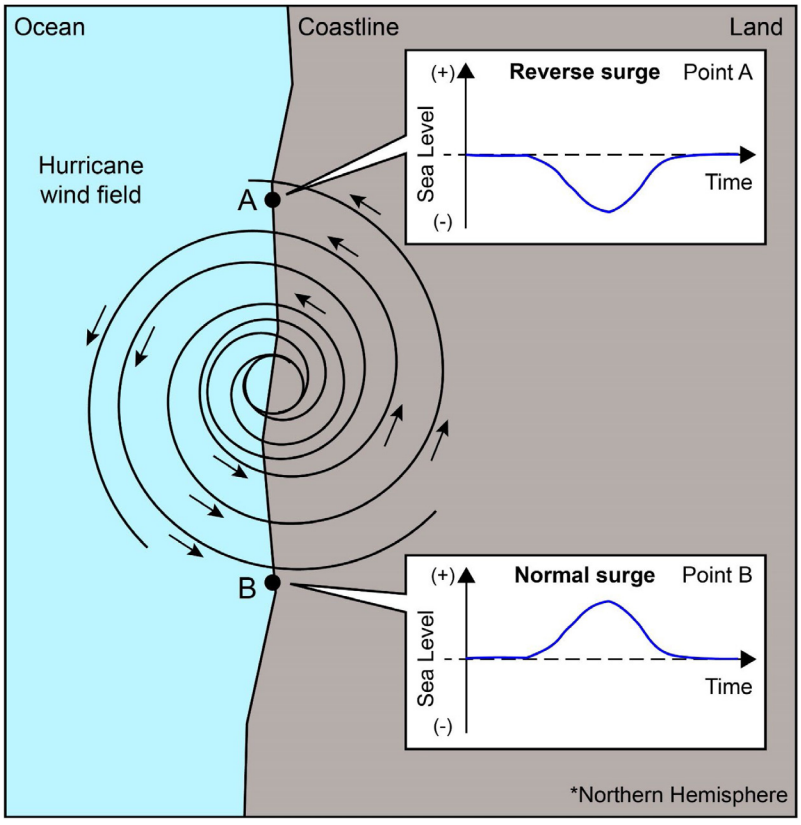

Fig. 2. Sketch showing normal (or positive — Point B), and reverse (or negative — Point A) storm surges generated by hurricane winds along different parts of a coast for a hurricane in the northern hemisphere.

water retreats towards the ocean (e.g., Jones and Davies, 2004 and Peng et al., 2006). Here, we name these two phenomena as normal (or positive) storm surge and reverse (or negative) storm surge (Fig. 2). Reverse surges appear to be less dangerous than normal surges as they do not generate coastal flooding, but in fact they pose some hazards in the form of damage to ships and boats due to the sudden and unexpected drops in coastal water levels, potential failures of the harbour bulkheads due to the absence of water pressure, damage to

Table 1
The list of atmospheric air pressure stations whose data are used in this research for studying the September 2022 Hurricane Ian. Abbreviations: NOAA, National Oceanic and Atmospheric Administration of the United States; ASOS, the Automated Surface Observing System.

Air pressure station name	Code	Longitude (°W)	Latitude (°N)	Sampling interval (min)	Source
Fernandina Beach	8720030	−81.47	30.672	6	NOAA
Apalachicola	8728690	−84.98	29.73	6	NOAA
Clearwater Beach	8726724	−82.832	27.978	6	NOAA
East Bay	8726674	−82.42	27.923	6	NOAA
Old Port Tampa	8726607	−82.553	27.858	6	NOAA
St. Petersburg	8726430	−82.627	27.762	6	NOAA
Port Manatee	8726384	−82.563	27.638	6	NOAA
Fort Myers	8725520	−81.87	26.65	6	NOAA
Naples	8725110	−81.81	26.132	6	NOAA
Vaca Key	8723970	−81.107	24.712	6	NOAA
Melbourne Regional	MLB	−80.645	28.103	1	ASOS
Mariana	MAI	−85.184	30.835	1	ASOS
West Palm Beach	PBI	−80.100	26.684	1	ASOS
Sanford/Orlando	SFB	−81.244	28.779	1	ASOS
Orlando International	MCO	−81.320	28.340	1	ASOS
Tampa Intl Airport	TPA	−82.540	27.962	1	ASOS
Hollywood//N. Perry	HWO	−80.241	26.000	1	ASOS
Fr. Pierce/St. Lucie	FPR	−80.377	27.498	1	ASOS
Miami Intl Airport	MIA	−80.317	25.788	1	ASOS
Jacksonville–Whitehouse	NEN	−81.867	30.349	1	ASOS
Mayport NS	NRB	−81.417	30.400	1	ASOS
Albany Municipal	ABY	−84.194	31.536	1	ASOS
Key West Nas	NQX	−81.689	24.576	1	ASOS
Tri Country	1J0	−85.601	30.846	1	ASOS
Sarasota–Bradenton	SRQ	−82.559	27.401	1	ASOS
Panama City (ECP)	ECP	−85.796	30.358	1	ASOS
Valdosta Regional	VLD	−83.274	30.776	1	ASOS
Brunswick/Malcolm	SSI	−81.391	31.152	1	ASOS
Ft. Myers/SW Florida	RSW	−81.757	26.538	1	ASOS
Fort Lauderdale	FXE	−80.170	26.200	1	ASOS
Daytona Beach Rgnl	DAB	−81.058	29.180	1	ASOS
Miami/Kendall-Tamia	TMB	−80.435	25.642	1	ASOS
Dothan Municipal	DHN	−85.450	31.320	1	ASOS
Key West	EYW	−81.760	24.556	1	ASOS
Pompano Beach	PMP	−80.111	26.246	1	ASOS
Apalachicola Muni	AAF	−85.027	29.728	1	ASOS
Saint Petersburg	PIE	−82.687	27.910	1	ASOS
Orlando/Herndon	ORL	−81.333	28.545	1	ASOS
Vero Beach Muni	VRB	−80.418	27.656	1	ASOS
Tallahassee Rgnl	TLH	−84.351	30.394	1	ASOS
Miami/Opa Locka	OPF	−80.283	25.910	1	ASOS
Jacksonville Intl	JAX	−81.688	30.494	1	ASOS
Winter Haven	GIF	−81.753	28.063	1	ASOS
Ft. Lauderdale/Holly	FLL	−80.150	26.070	1	ASOS
Jacksonville/Craig	CRG	−81.513	30.337	1	ASOS
Gainesville Rgnl	GNV	−82.276	29.692	1	ASOS
Leesburg Municipal Airport	LEE	−81.810	28.820	1	ASOS
Jacksonville Nas	NIP	−81.675	30.234	1	ASOS
Saint Petersburg	SPG	−82.627	27.765	1	ASOS

coastal ecosystems, as well as potential health and safety concerns for local people in case they decide to walk on the muddy exposed seafloor. It is important to note that reverse surges can have catastrophic consequences for some coastal industries that heavily rely on ocean water such as nuclear power plants (e.g., Needham, 2022). Therefore, it is critical to understand the mechanism behind the generation of reverse storm surges and to be able to predict them.

The normal and reverse storm surges are the results of the combined actions of air pressure drop, wind and the geometries of the coast and water body (Fig. 2). While pressure drop on the ocean surface usually causes the water level to swell and leads to normal surges, winds can cause both normal and reverse surges depending on the direction of the wind. Landward winds are expected to cause normal surges whereas seaward winds may result in reverse ones; winds occurring parallel to coasts may cause both types of surges due to the Ekman transport (Weisberg and Zheng, 2006). Therefore, the shape of the surge (either normal or reverse) is the outcome of the interactions among the aforementioned three participating factors. We know that hurricanes rotate counter-clockwise in the northern hemisphere. Referring to Fig. 2, the wind blows landward in point A generating normal storm surge. However, the wind direction is opposite in point B resulting in reverse storm surge.

The reverse storm surge is rarely reported or analysed because a relatively dense network of tide gauges is required to sight both normal and reverse storm surges. For the case of September 2022 Hurricane Ian in Florida, such a relatively dense network of tide gauges is available which enabled us to study the normal and reverse storm surges. Previous studies that reported reverse storm surges are Jones and Davies (2004), Peng et al. (2006) and Chen et al. (2018). However, these studies did not discuss the mechanism responsible for the generation of the reverse surges. Therefore, there are two research gaps in this field which are (1) few studies reported reverse storm surges, and (2) no study was conducted on the generation mechanism of this phenomenon. Considering these research gaps, we designed this research to address the generation mechanism of reverse surges for the first time. Here, we used a large dataset including air pressure, wind velocity, and sea level tide gauge data to study the event through a hybrid approach combining data analysis and numerical modelling.

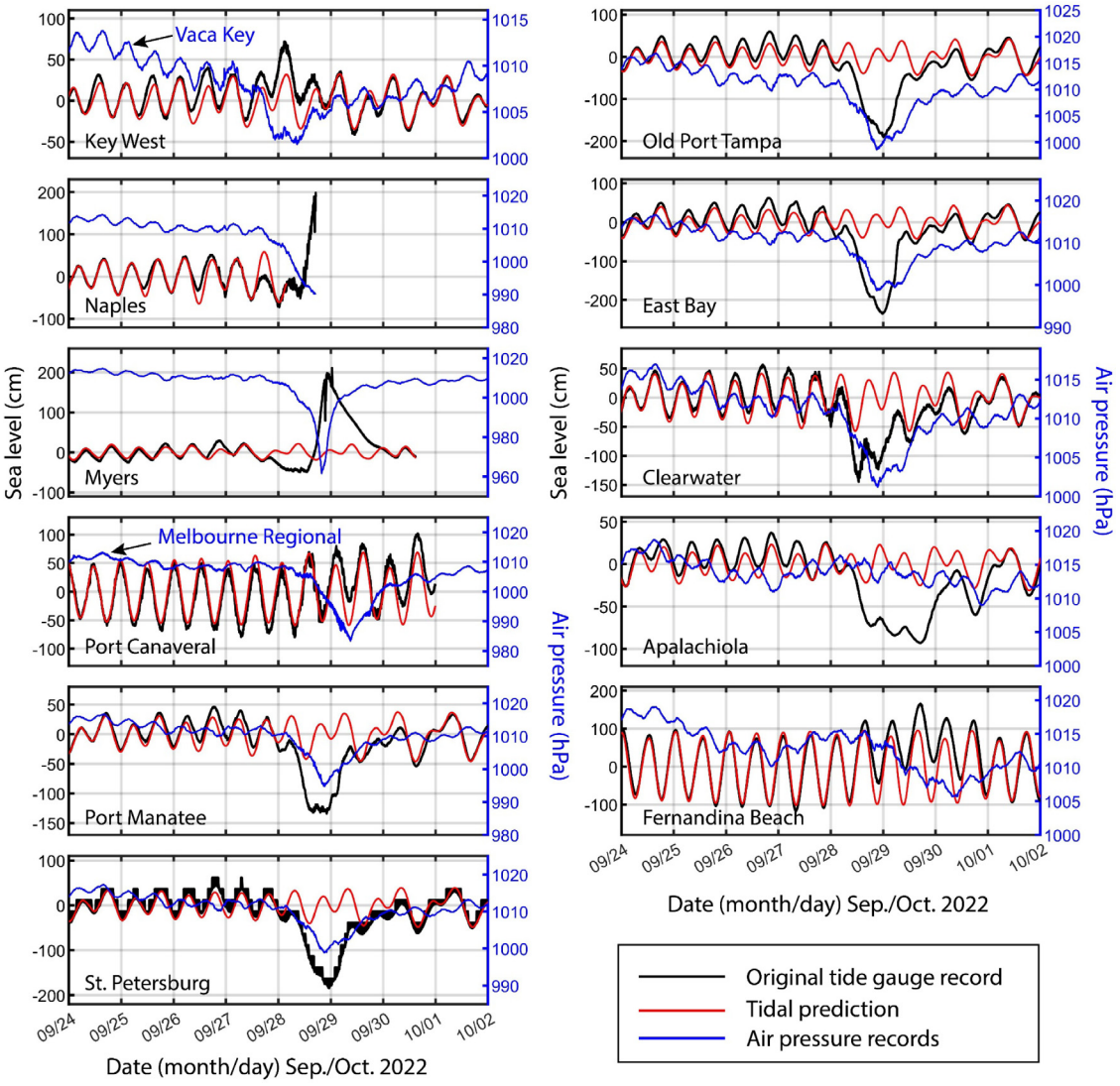

Fig. 3. The original tide gauge records (black), predicted tides (red) and original air pressure records (blue) at stations along the track of the September 2022 Hurricane Ian. The locations of the stations are shown in Fig. 1. Both tide gauge and air pressure data are from the NOAA network. Exception is Melbourne Regional air pressure data which is from the ASOS network.

Table 2
The list of 11 tide gauge stations whose data are used in this research for studying the September 2022 Hurricane Ian.

Tide gauge station name	Longitude (°W)	Latitude (°N)	Sampling interval (min)
Fernandina Beach	−81.47	30.672	1
Apalachicola	−84.98	29.73	1
Port-Canaveral	−80.593	28.415	1
Clearwater Beach	−82.832	27.978	1
East Bay	−82.42	27.923	1
Old Port Tampa	−82.553	27.858	1
St Petersburg	−82.627	27.762	1
Port Manatee	−82.563	27.638	1
Fort Myers	−81.87	26.65	1
Naples	−81.81	26.132	1
Key West	−81.808	24.553	1

2. Data and methods

Meteorological data were downloaded from the Tides and Currents NOAA portal (National Oceanic and Atmospheric Administration of the United States; https://tidesandcurrents.noaa.gov/) and the ASOS network (the Automated Surface Observing System; https://mesonet.agron.iastate.edu/request/asos/1~min.phtml#) (Table 1). The analysed data from the NOAA stations (Fig. 1 and Table 1) includes air pressure, wind speed, and wind direction; all of which were measured with a 6-min time step. The examined ASOS network stations (Fig. 1 and Table 1) came with sampling intervals of 1 min and include air pressure, wind speed, and wind direction. All air pressure and wind speed series were quality checked and unrealistic spikes were removed.

Eleven tide gauge records are used in this study which are provided by the Center for Operational Oceanographic Products and Services (CO-OPS) of NOAA (https://tidesandcurrents.noaa.gov/tsunami/#). All tide gauge data have a sampling interval of 1 min (Table 2). After data quality control (removing spikes; e.g. Wang et al., 2022), tidal analysis was conducted applying the TIDALFIT tide package (Grinsted, 2008), which is based on using ordinary least-squares technique to calculate tidal components. TIDALFIT is a powerful tidal tool and has been used in numerous studies in the past (e.g., Heidarzadeh et al., 2022, 2017). After calculating the tidal signals for each tide gauge record, they were removed from the original tidal records to obtain detided records (Fig. 3). To calculate the surge signals, we applied a moving average filter with window length of 30 min on the detided records. While a band-pass filter also could be used for extracting the surge signals, we preferred a 30-min moving-average filter in this study

Table 3
The domains, grid sizes, and the domain-dependent settings of the nested grid system used in this study for modelling the storm surges generated by September 2022 Hurricane Ian.

Grid name	Spatial coverage (deg.)		Grid spacing (m)	Baroclinic/Barotropic time steps (s)	Horizontal viscosity coefficient (m^2/s)
D1	Lon: Lat:	101.33°W–66.89°W 5.12°N–37.31°N	25,000	20/2	100
D2	Lon: Lat:	85.27°W–78.42°W 23.65°N–32.81°N	5000	5/0.5	50
D3	Lon: Lat:	83.33°W–81.13°W 25.72°N–28.55°N	1000	1/0.1	30

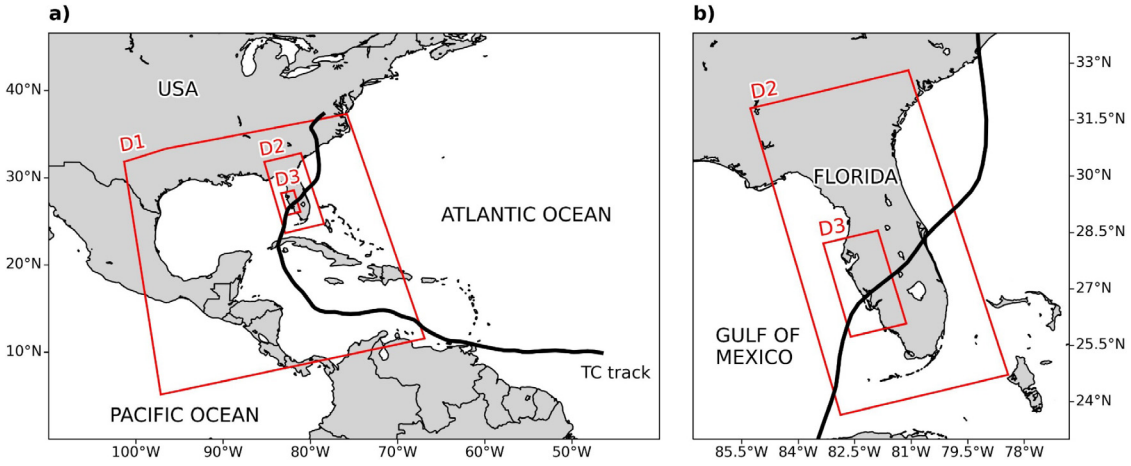

Fig. 4. The three-level nested grid system used for modelling the September 2022 Hurricane Ian. The grid spacings are 25,000 m for D1, 5000 m for D2, and 1000 m for D3. The thick black line shows the track of the hurricane. TC indicates Tropical Cyclone.

as it is an optimum filter for reducing noise in the time domain. The 30-min time window proved efficient in extracting surge signals in the past studies considering the storm surge periods of one to two days (e.g., Heidarzadeh et al., 2018; Le et al., 2019 and Heidarzadeh and Rabinovich, 2021). In Naples, the tide gauge stopped working during the hurricane and thus a full picture of the storm surge at this station is unavailable (Fig. 3). As a result, a full tidal prediction spanning the hurricane period is not possible at this station. Therefore, the direct sea level record is approximated as the storm surge at this station.

According to Fig. 3, although there is a significant air pressure drop at all stations around the beginning of 29th September 2022, except for Apalachicola, some stations experienced normal (positive) surge (e.g., Naples and Myers) while others faced reverse (negative) surges (e.g., Port Manatee and Claerwater). This unusual observation is studied in detail in the next sections through analysis of various meteorological data and modelling. To analyse synoptic situation in a wider area, ERA5 global reanalysis atmospheric data (10-m wind velocity and mean sea level pressure) (Hersbach et al., 2020) were downloaded and analysed from the (Copernicus Climate Change Service, 2017) database.

To further study the generation mechanisms of the normal and reverse surges, storm surge hindcasts were performed using the Regional Oceanic Modelling System, known as ROMS (Shchepetkin and McWilliams, 2005). The computational domains were composed of three nested grids (Table 3, Fig. 4). The horizontal grid sizes were 25,000 m in the outermost grid (D1) covering the entire Gulf of Mexico, 5000 m for the middle grid (D2), and 1000 m in the innermost grid (D3). The D3 grid was set to capture the normal and reverse surges in a single domain. The bathymetric grids used for conducting the hindcasts were made using the GEBCO_2022 bathymetric database (Weatherall et al., 2015). In the vertical direction, the grids were divided into 10 layers (Table 3). The hindcasts were firstly conducted in grid D1 from 00:00 UTC on 25th September to 23:00 UTC on 30th September to make the initial and boundary conditions for the grids D2 and D3. Later, the storm surges in these grids were simulated for about 86 h from 00:00 UTC on 26th September using the two-way nesting method (Heidarzadeh et al., 2021).

To simplify the computational settings, phenomena such as astronomical tides, wave set-up, and the effect of waves were excluded in the modelling process, and seawater temperature and salinity were set as constant values of 26.5 °C and 34.5 PSU, respectively. As our tide gauge data have sampling intervals of 1 min (Table 2), they do not properly record the waves and thus do not allow us to study the waves. We note that the sampling intervals of the data should be at least 1 s to allow proper recording and analysis of waves during a hurricane (e.g., Musinguzi and Akbar, 2021). Therefore, waves were not modelled in this study. Wave set-up may increase mean sea level (e.g., Heidarzadeh et al., 2009). However, since Tampa Bay and the Florida Keys are semi-enclosed bays with shallow water, wave heights tend to be smaller than those in the open ocean and thus wave set-up is expected to be negligible. The tide-surge interaction is a decisive parameter regarding coastal flooding (e.g., Rego and Li, 2010) as surges occurring at high tides would cause more intense coastal flooding and vice versa. However, coastal flooding was out of the scope of this study and thus we did not consider tide-surge interaction.

In our simulations, the 10-m wind and sea level pressure fields from the parametric model (PM) of tropical cyclones (Holland, 1980; WMO, 2011) and a numerical weather prediction model (NWP) were independently used as the atmospheric forcings. As for the NWP, the High-Resolution Rapid Refresh (HRRR) provided by NOAA (Benjamin et al., 2021) was employed in the hindcast near the Florida coasts. For the larger domain covering the entire Gulf of Mexico and the Caribbean Sea, data from a coarser Rapid Refresh (Benjamin et al., 2016) was used. Thus, two independent hindcasts were obtained using these two types of atmospheric inputs (i.e., PM and HRRR). The results are described in Section 6 of this article. We obtained the hurricane best track data, which is required as inputs for the PM model, from the International Best Track Archive for Climate Stewardship (IBTrACS)

Table 4
Comparing the three databases of wind and pressure data used in this study in terms of spatial resolution and other parameters.

Dataset	Type	Scale	Temporal and spatial resolution	Source of data
ERA5	Reanalysis	Global	30 km and 1 h	https://cds.climate.copernicus.eu/cdsapp#!/home
HRRR	Forecast	Regional	3 km and 1 h	https://rapidrefresh.noaa.gov/
PM	Parametric	Regional	Adjustable	The equations by Holland (1980) with inputs from IBTrACS dataset (Knapp et al., 2010, 2018) (https://www.ncei.noaa.gov/products/international-best-track-archive)

Table 5
Comparison of measured wind speed with that from three models of HRRR, PM and ERA5 at the location of tide gauges during the September 2022 Hurricane Ian. "max." and "min." represent maximum and minimum.

Station name	Measured max. wind speed (m/s)/min. pressure (hPa)	Model max. wind speed (m/s)/min. pressure (hPa) from HRRR	Model max. wind speed (m/s)/min. pressure (hPa) from PM	Model speed/pressure from ERA5 (m/s)
Fernandina Beach	13.9/1005.7	13.1/1005	7.4/1007	13.8/1004.5
Apalachicola	13.3/1009	9.4/1009	1.6/1009	9.9/1008.4
Port Canaveral/Melbourne Regional[a]	40.0/983.4	17.9/990	23.4/987	13.4/992.5
Clearwater Beach	23.1/1001.2	18.2/1002	14.5/1007	19.6/1000.0
East Bay/Old Port Tampa[a]	19.5/998.7	14.9/1000	20.9/1004	14.4/999.1
Old Port Tampa	19.5/998.6	19.6/1000	19.2/1005	15.9/996.4
St. Petersburg	18.9/998.9	19.0/999	21.8/1004	20.4/997.8
Port Manatee/St. Petersburg	18.9/994.8	22.1/996	24.7/1002	15.9/996.4
Fort Myers	25.7/961.6	22.4/968	56.3/970	13.8/985.0
Naples	25.0/990.2	20.8/991	35.7/999	20.4/988.9
Key West/Vaca Key[a]	15.4/1001.5	25.1/998	23.1/100	20.7/1002.2

[a]Indicates that atmospheric data of pressure drop and wind speed are missing at the location of the corresponding tide gauge stations, and thus those data are taken from the closest station (marked by a star at the first column).

(Knapp et al., 2010, 2018). The 10-m wind speed was converted to the wind stress (τ_s) using the following equation before the hindcasts:

$$\tau_s = \rho_a C_D V^2 \tag{1}$$

where τ_s is wind stress, ρ_a is air density (= 1.1 kg/m^3), C_D is the surface drag coefficient, and V is the 10-m wind speed (m/s). C_D was estimated using the following equation, which is one of the classic equations based on a wind speed threshold (Mitsuyasu and Honda, 1982; Nakamura et al., 2019):

$$C_D = \begin{cases} \left(1 - 1.89 \times V \times 10^{-2}\right) \times 1.28 \times 10^{-3} & V < 8 \text{ m/s} \\ \left(1 + 1.078 \times V \times 10^{-1}\right) \times 5.81 \times 10^{-4} & 8 \text{ m/s} \le V < 30 \text{ m/s} \\ 2.46 \times 10^{-3} & 30 \text{ m/s} \le V \end{cases} \tag{2}$$

Since Eq. (2) is a function of wind speed, the surface stress can be affected by the topography through the wind field variations, and wind speed reductions due to land. It is noted that sea surface stress in PM does not consider the effects of topography since PM cannot consider these effects physically.

It can be seen that three different types of wind and pressure data are collected and analysed in this study for different purposes in order to provide a holistic analysis and modelling of Hurricane Ian (Table 4). They are classified into two groups: global (ERA5 reanalysis data), and regional (HRRR and PM) data. Obviously, these datasets offer varied degrees of resolutions and uncertainties. While regional datasets (HRRR and PM) offer higher resolution data, global data of ERA5 come with lower resolutions as it is naturally expected for any global dataset. Table 4 compares these three databases of wind and pressure data in terms of spatial and temporal resolution and other parameters. Table 5 compares the maximum wind speed and minimum air pressure at the location of tide gauges from these three datasets. According to Table 5, wind and pressure values from various dataset are separated by up to approximately 84% and 1%, respectively, from one dataset to another in some stations. The purpose for using global data of ERA5 was to study the propagation of Ian on a wide region and to provide a general global understanding of Ian's propagation whereas regional data were used as inputs for the ocean model.

Referring to Table 5, it is noted that the PM gives a relatively high speed of 56.3 m/s in Fort Myers. This can be attributed to the nature of the PM model which does not take into account wind speed reduction due to ground or sea surface friction. Therefore, PM models are more reliable over sea and appear less reliable onshore and on land.

3. Analysis of atmospheric pressure changes

Air pressure evolution related to propagation of Hurricane Ian over Florida is shown in Fig. 5. We present air pressure series measured at stations located along the propagation direction (up to ±100 km from the centre of the track) (Fig. 5a), and at stations located along the cross-propagation direction (up to approximately ±250 km from the centre of the track) (Fig. 5b). Looking at Fig. 5, Hurricane Ian's high spatial and temporal variability is instantly noted. What sets Hurricane Ian apart from other North Atlantic hurricanes is that it made landfall as a Cat −4 hurricane, whereas most hurricanes typically significantly lose power before landfall. Along the west coast of Florida, at Fort Myers station (station 8725520, Fig. 5a), approximately at the location where Ian reached the coast (Fig. 1), air pressure dropped for 50 hPa within approximately 24 h, reaching a minimum value of 961.6 hPa at 19:48 UTC on 28th September. Approximately 100 km to the northwest, at Sarasota–Bradenton (SRQ, Fig. 5a), the rate of air pressure drop was less than half of that (18.9 hPa/day), and the lowest measured pressure was 990 hPa. While propagating towards northeast, Ian swiftly downgraded over the land. By the time it reached the eastern coast of Florida, it was a Cat −1 hurricane, with an air pressure drop rate of approximately 25 hPa/day. A minimum air pressure of 983 hPa was measured at Melbourne Regional (MLB, Fig. 5), located at the right side of the track. To the northwest and southeast of the track, at distance of ±250 km, only a weak air pressure drop was measured: ~3.0 hPa/day at Jacksonville Intl (JAX, Fig. 5b), and ~4.2 hPa/day at station Miami/Kendall-Tamia (TMB, Fig. 5b), with air pressure values keeping relatively high values of 1005 hPa (JAX), and 1003 hPa (TMB). As it found itself once again over the ocean, which acts as a source of

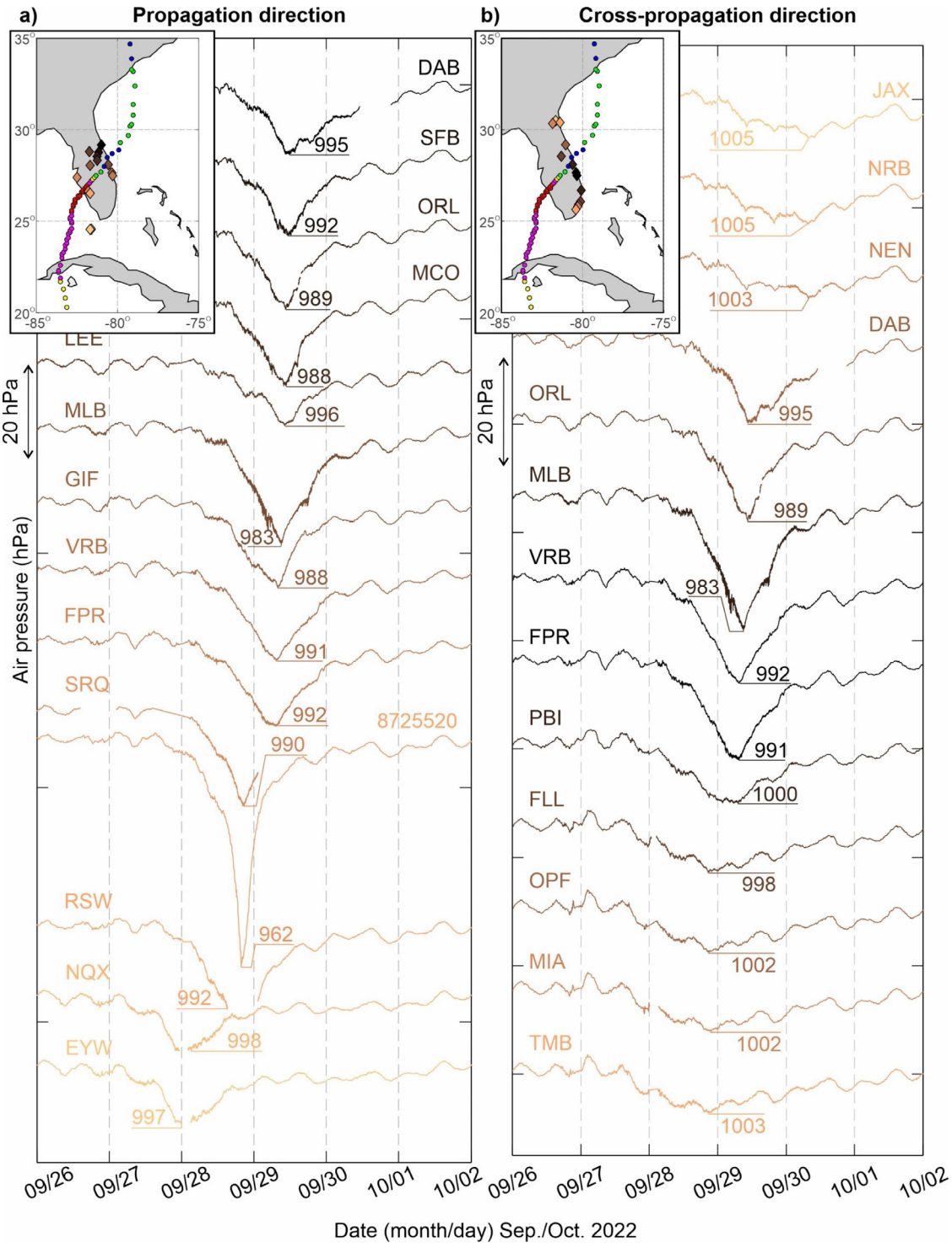

Fig. 5. Air pressure time series measured at meteorological stations along: **(a)** propagation; and **(b)** cross-propagation direction of Hurricane Ian. Data are provided by the ASOS network and NOAA. Station locations are shown in two insets, along with Hurricane Ian propagation track (see Fig. 1 and Table 1 for location of stations). The ASOS and NOAA station names and their abbreviated codes are provided in Table 1.

heat and vapour necessary for maintenance and growth of hurricanes (Emanuel, 2003), Ian restrengthened to a Cat −2 hurricane in east of Florida and over the Atlantic Ocean. Upon reaching the coast of South Carolina, and moving back over the land, it downgraded to Cat −1. Regarding the minimum pressure values and area over which it was observed, Ian can be considered as a typical hurricane. According to the ERA5 data, radii of Hurricane Ian outermost closed isobar (ROCI), which is a parameter commonly used to measure overall hurricane size (Merrill, 1984), was approximately 300 km. The ROCI mean and standard deviation values for the North Atlantic hurricanes have previously been estimated as 333.0 ± 155.4 km (estimated for 1957–1977; Merrill, 1984) and 351.9 ± 122.0 km (estimated for 1988–2002; Kimball and

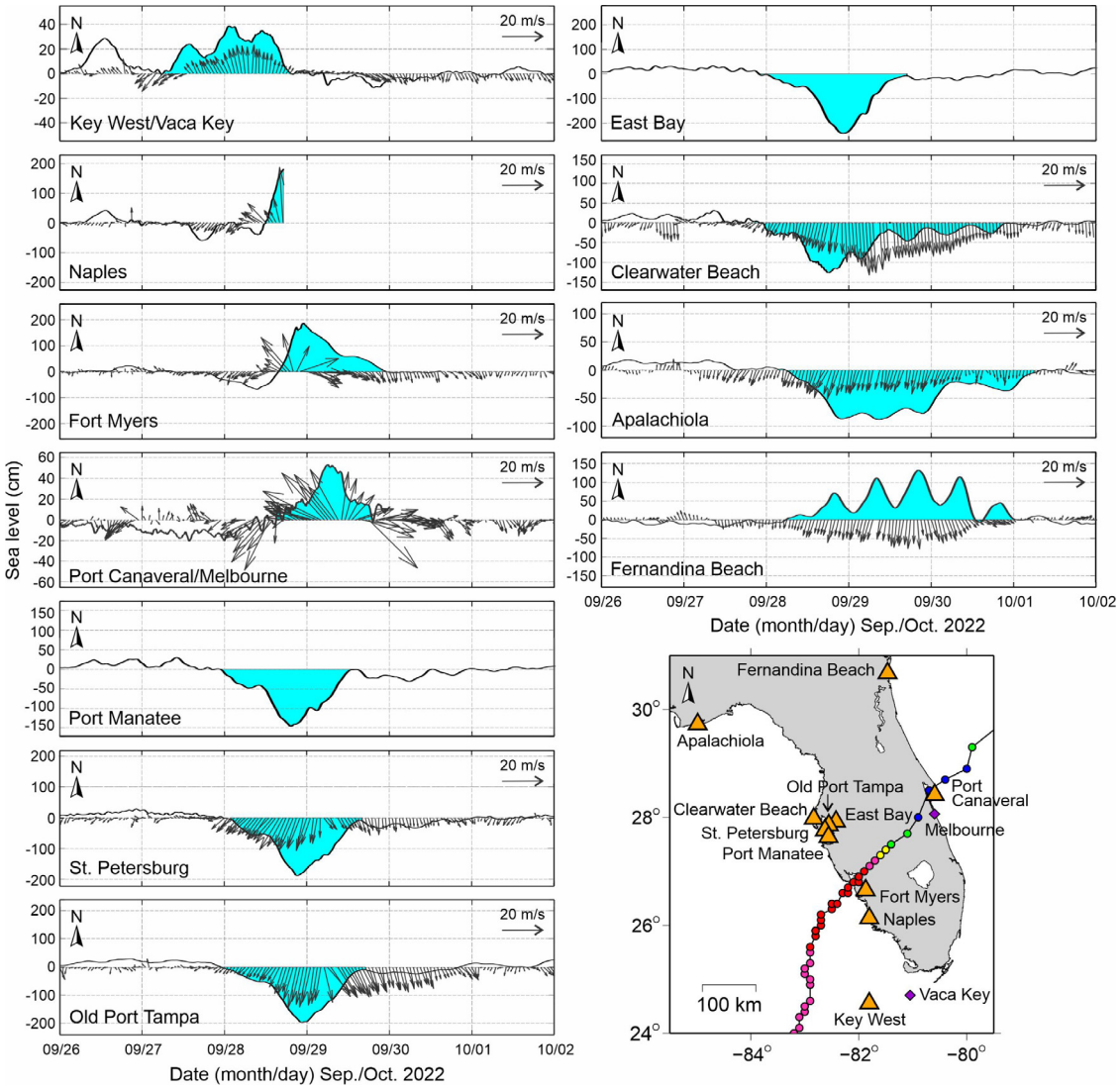

Fig. 6. Storm surges generated by the September 2022 Hurricane Ian overlaid by the hurricane 10-m wind velocity measurements (shown by arrows) gathered at NOAA and ASOS stations. The velocity arrows show 10-m wind measured speed magnitudes and directions relative to North. The north directions are indicated in all panels.

Mulekar, 2004). Minimum measured pressure associated with Hurricane Ian is also in line with minimum pressure values associated with the North Atlantic Cat −4 hurricanes (Landsea, 1993).

4. Storm surges generated by Hurricane Ian

Storm surges generated by Ian are shown in Fig. 6 by shaded areas, along with measured winds at the NOAA/ASOS stations. Out of the 11 stations examined here, five of them registered normal surges while the other six stations recorded reverse surges. The maximum amplitude of normal surges varies from 0.4 m to over 1.8 m whereas it was in the range of 0.9 m–2.4 m for reverse surges (Table 6). The largest normal surge was observed in Naples (>1.8 m; the exact amplitude is unknown since the instrument was broken during the hurricane) and Fort Myers (1.8 m) which are the closest stations to the hurricane track. These are also highest values on record for both stations (NOAA, 2022). The maximum reverse surges belong to East Bay (2.4 m) and Old Port Tampa (2.0 m) located inside the Tampa Bay. Duration of storm surges ranged from 1.2 days in Port Canaveral to 3.0 days in Apalachicola (Table 6, Fig. 6). It may be inferred that the amplitudes of reverse surges were larger than those of normal surges. According to Table 6 and Figs. 6–7, all cases of normal and reverse surges were consistently generated by landward and seaward winds, respectively. In Fig. 6, the directions indicated by wind velocity arrows are indicated relative to north, where the north direction is given in each plot. For example, for the case of Fernandina Beach (Fig. 6), the velocity arrows indicate dominant southward winds at this station, which means wind was mostly blowing landward in Fernandina Beach during the hurricane.

Although storm surges are generated by the joint action of hurricane's pressure drop, wind velocity field and the geometrical features of the coastal areas and water bodies, this data, along with air pressure data (Table 6, Fig. 5) reveals that wind played a dominant role over air pressure drop to generate reverse surges during Ian. Namely, at locations which experienced reverse surges, wind acted for lowering the sea level, whereas air pressure operated towards rising the sea level. At locations which experienced normal surges, both wind and air pressure acted in the same direction.

To better visualize the interactions of air pressure drops and winds towards the generation of the storm surges, we also plot the variations of both parameters during the propagation of Ian at 12 h intervals using ERA5 global reanalysis data (Fig. 7). It can be seen that positive storm surges were generated at coastal locations where wind was blowing landward: along Florida Keys (Key West and Vaca Key) during 00:00–12:00 UTC on 28th September, then along the southwest Florida coast from 12:00 UTC on 28th September to 12:00 UTC on 29th September,

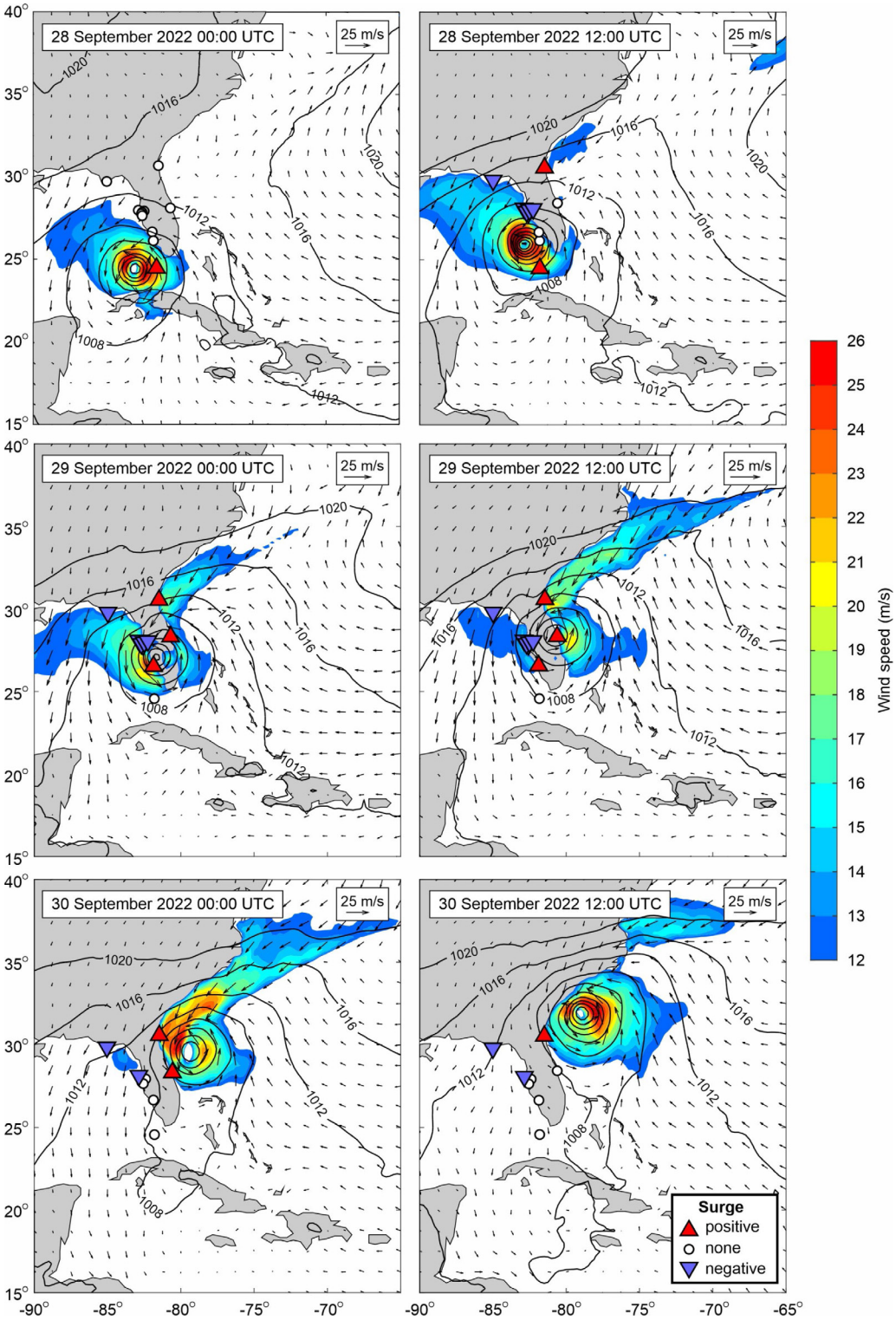

Fig. 7. Propagation of September 2022 Hurricane Ian from Gulf of Mexico to Florida and the Atlantic Ocean. Shown are temporal evolution of mean sea level pressure (black contours), wind velocity (vectors and filled contours — here only speeds above 12 m/s are coloured), and characteristic of the surge signals (positive, none, or negative) at the NOAA stations. Data are based on the ERA5 global reanalysis.

and finally along the east Florida coast during 30th September. Negative surges were generated along those parts of the coast over which wind was blowing seaward, in particular over the northwest coast of Florida. Negative surges apparently lasted longer, that is from midday hours on 28th September up to 18:00 UTC on 30th September.

It should be noted that ERA5 global reanalysis fails to reproduce hurricanes in their full strength. Minimum mean sea level air pressure related to Hurricane Ian reproduced by the ERA5 data is approximately 975 hPa, which is 13 hPa higher than the minimum recorded mean sea level pressure of 961.6 hPa (Fig. 5). Likewise, maximum coastal

Table 6
Characteristics of storm surges generated by the September 2022 Hurricane Ian at tide gauge stations along the coast of Florida.

Station name	Type of surge	Wind direction	Maximum observed surge amplitude (m)	Surge duration (day)	Pressure drop (hPa)	Maximum wind speed (m/s)
Fernandina Beach	Normal	Landward	1.3 ± 0.1	2.7	5.2	13.9
Apalachicola	Reverse	Seaward	0.9 ± 0.1	3.0	5.1	13.3
Port Canaveral/Melbourne Regional[a]	Normal	Landward	0.5 ± 0.1	1.2	23.0	40.0
Clearwater Beach	Reverse	Seaward	1.2 ± 0.1	2.9	10.8	23.1
East Bay/Old Port Tampa[a]	Reverse	Seaward	2.4 ± 0.2	1.7	12.9	19.5
Old Port Tampa	Reverse	Seaward	2.0 ± 0.2	1.7	13.2	19.5
St. Petersburg	Reverse	Seaward	1.9 ± 0.2	1.6	12.7	18.9
Port Manatee/St. Petersburg	Reverse	Seaward	1.4 ± 0.2	1.6	16.3	18.9
Fort Myers	Normal	Landward	1.8 ± 0.1	1.3	50.0	25.7
Naples	Normal	Landward	>1.8	N/A	19.9	25.0
Key West/Vaca Key[a]	Normal	Landward	0.4 ± 0.1	1.5	6.4	15.4

[a]Indicates that atmospheric data of pressure drop and/or wind speed are missing at the location of corresponding tide gauge stations, and thus those data are taken from the closest station (marked by a star at the first column).

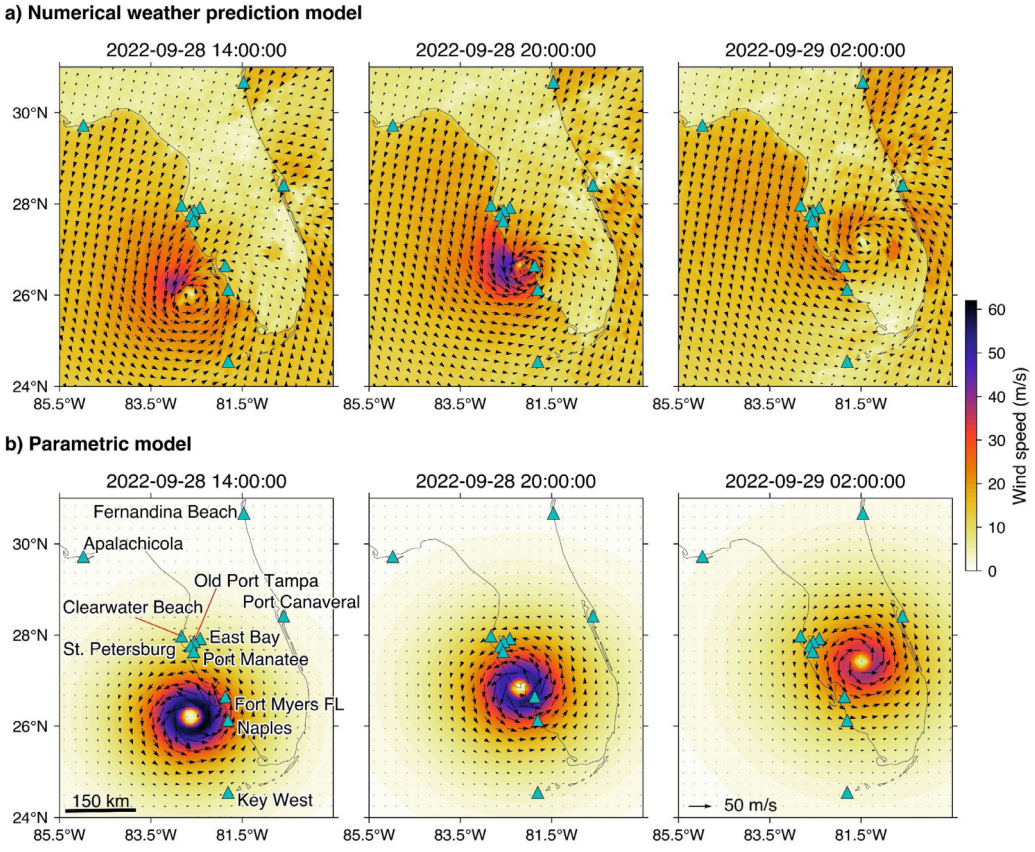

Fig. 8. Wind speed field over Florida during the passage of September 2022 Hurricane Ian at different times based on the NWP model **(a)** and the parametric typhoon model (PM) **(b)**. Time units are in UTC. The NWP model is based on the HRRR model of NOAA and PM model is simulated using the formula by Holland (1980).

10-m wind reproduced by ERA5 is ~30 m/s which is lower than the maximum measured coastal 10-m wind of 40 m/s. The discrepancies are likely related to the fact that the resolution of global models (A grid of 0.25° ×0.25° for ERA5) is inadequate for reproducing the observed data and their variations (e.g., Slocum et al., 2022).

5. Wind speed field using regional data

The temporal evolutions of the wind speed field generated by Hurricane Ian are plotted in Fig. 8 using two independent regional models: a numerical weather prediction model (NWP) and a parametric wind model (PM). In general, the pattern sketched in Fig. 2 can be seen in the wind speed field of both models for Hurricane Ian: the stations to the northwest of the eyewall (e.g., Port Manatee) are under an oceanward wind field and thus experience reverse surges, while those located southeast of the eyewall (e.g., Naples) experience landward winds leading to normal surges (Figs. 6 and 8).

Although the general wind field patterns are similar for the NWP and PM models, they slightly differ in predicting wind intensities. The NWP model incorporates topographic effects on the wind intensities, thus resulting in a more complex and realistic structure of wind fields (Fig. 8a) compared to the PM model (Fig. 8b). However, NWP models typically cannot accurately resolve the hurricane track and intensity, particularly near the hurricane centre (Rahman et al., 2022). Our result shows that the maximum wind speed by the NWP model amounts to approximately 50 m/s, which is lower than that from the PM model around the eyewall (approximately 60 m/s). Consequently, the PM model is favourable over the NWP model for predicting the storm

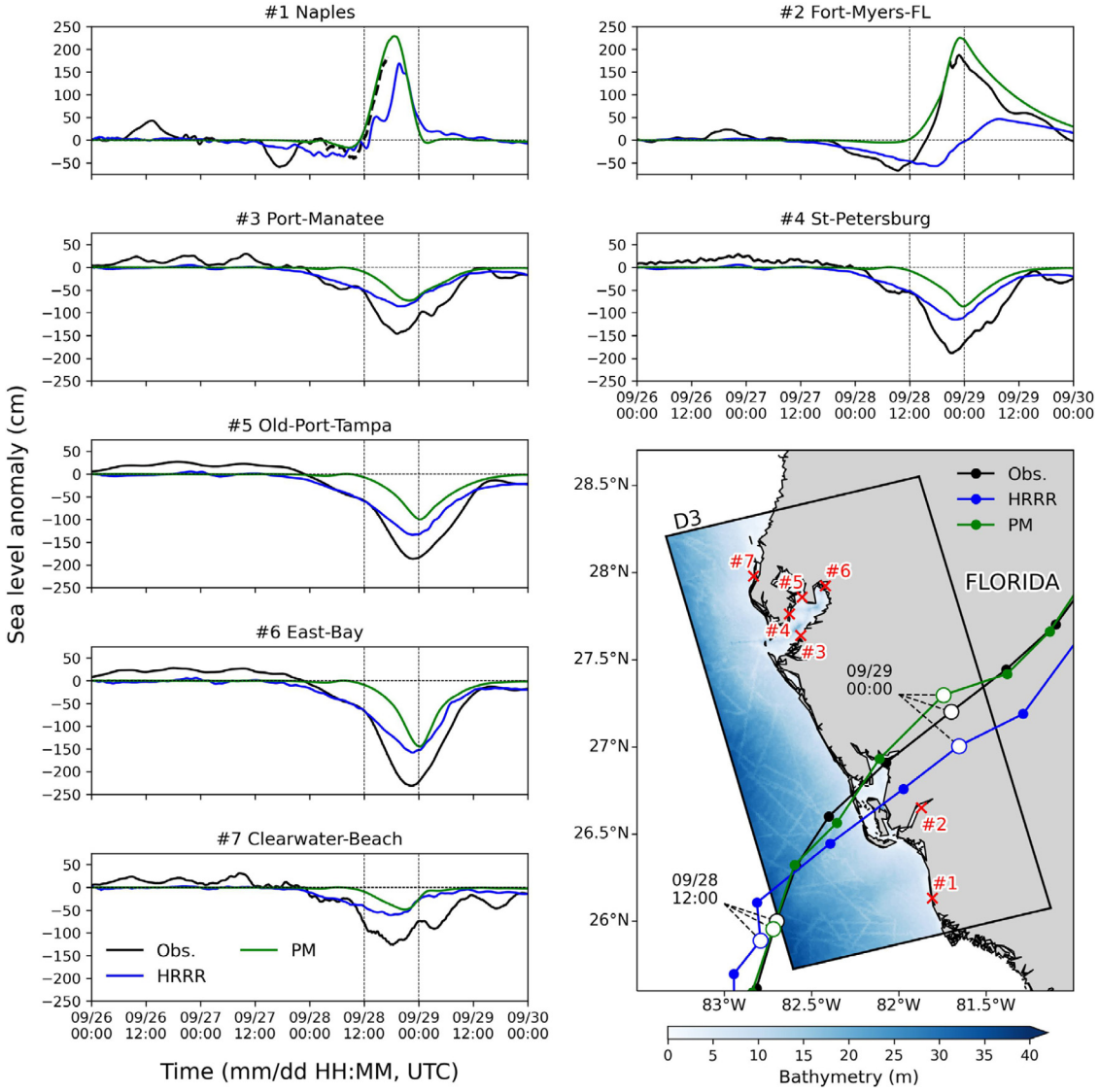

Fig. 9. Comparison of the observed (black) and simulated (blue for HRRR and green for PM) storm surge waveforms for the September 2022 Hurricane Ian. The bathymetry used for modelling (D3) is also shown. Note that the time series of sea level anomaly around the maximum in Naples (the dashed line) was not the detided record due to the aliasing in the tidal prediction.

surge at stations close to the hurricane track. In comparison to the ERA5 global data, it can be seen that both regional models give higher maximum wind speeds than the ERA5 global dataset (30 m/s). These results are in line with previous studies comparing PM and NWP models for storm surge modelling (Toyoda et al., 2022; Rahman et al., 2022; Mulia et al., 2023).

6. Numerical modelling and validation

The time series of the simulated sea level changes during Hurricane Ian are compared to those of the observations in Fig. 9. Simulations were performed using two independent sets of input parameters: the parametric model (PM, Fig. 9, green) and the High-Resolution Rapid Refresh (HRRR, Fig. 9, blue). In general, the simulations are successful in reproduction of the pattern of the storm surges, either normal or reverse. However, there are differences between the simulated and observed surge amplitudes. For the tide gauge stations near the hurricane track which are under landward winds (i.e., Naples and Fort Myers), normal surges were observed and were successfully simulated during the hurricane passage (12:00 UTC on 28th September to 0:00 UTC on 20th September), as expected. At Naples, both maxima of the simulated surges using HRRR and PM models were more than 150 cm where the surge from the PM model was approximately 50 cm higher than the HRRR model. The notable difference between HRRR and PM simulations is exhibited in Fort Myers, which is located near the hurricane track. The HRRR simulation underestimates the observation by more than 100 cm although the observation was reproduced well using the PM simulation. This could be explained by the weaker intensity of the hurricane winds in the HRRR model as compared to the PM model (Table 5; Fig. 8). In addition, the track errors in the HRRR model may also have contributed to this underestimation, especially since it appears that the hurricane eye passed over Fort Myers in the HRRR model. In contrast, the reverse surges observed in Tampa Bay (stations #3 to #7 in Fig. 9) were better reproduced by the HRRR model. Since the Tampa Bay is relatively far from the hurricane track (a distance of approximately 125 km), the wind speed from the HRRR model was anticipated to be more accurate than that in the PM model, resulting in a smaller discrepancy with the observed surges. In fact, the wind field in the PM model did not show the spatial variability induced by land, and the wind speed around the bay was generally weaker than that in the HRRR model (see Fig. 8).

The spatiotemporal distributions of the sea level anomalies offer further insights on the propagation of Ian's storm surges (Figs. 10–12).

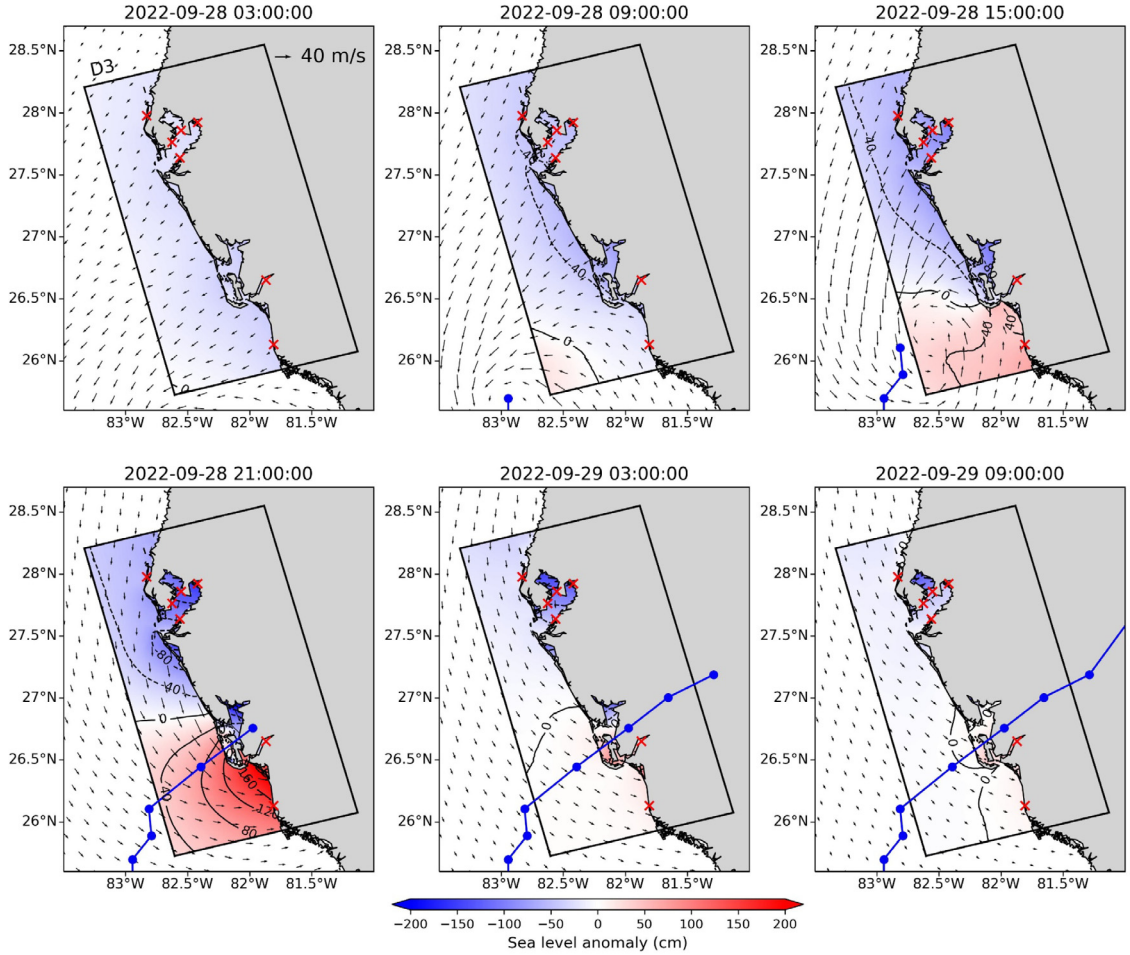

Fig. 10. Snapshots of simulated storm surge propagation during the September 2022 Hurricane Ian at 6 h intervals based on input data from the High-Resolution Rapid Refresh (HRRR) program of NOAA. The location of the central position of Hurricane Ian based on the HRRR data is also shown (blue line). The vectors represent the wind fields based on the HRRR data.

In the HRRR model, even when the hurricane was located offshore (Fig. 10, from 03:00 UTC to 09:00 UTC on 28th September), the sea level decreased over the entire grid D3 leading to reverse surges. At that time, the south-westward wind, which was favourable to cause decrease in sea level, was dominant near the coast as indicated by arrows in Fig. 10. As the hurricane approached the shoreline, the normal surges occurred rightward of the track, and the reverse surges occurred leftward simultaneously with respect to the forwarding direction of the hurricane. Since the maximum increase in sea level due to the pressure drop (i.e., the inverse barometer effect) is estimated to be approximately 50 cm using the observed pressure drop in Fort Myers from 1011.6 hPa to 961.6 hPa (Fig. 5), we may conclude that the southerly to westerly wind fields at the right side of the hurricane (Fig. 9) were the primary factor for the generation of the normal surges.

In addition, the south-westward winds were maintained in Tampa Bay when the hurricane made landfilled. Consequently, the entire sea level in domain D3 gradually approached the still-water level after landfall (Fig. 10). Such spatiotemporal evolution of sea level anomalies is confirmed by the PM simulations (Fig. 11). As expected, the larger amplitudes of the normal and reverse surges were simulated more accurately by the PM model for areas near the hurricane's centre, as compared to the simulation results using the HRRR model (Fig. 9).

To further examine the mechanism for the occurrences of normal and reverse surges, the depth-averaged momentum balance was analysed for the case of using the realistic forcing of HRRR, as per Weisberg and Zheng (2006). Assuming a uniform sea water density ρ_w (kg/m^3), the same as in the setting of the hindcast, the momentum balance in the Cartesian coordinates can be written as follows:

$$\underbrace{\frac{\partial \bar{u}}{\partial t}}_{ACC} + \underbrace{(\bar{u}\cdot\nabla)\,\bar{u}}_{ADV} + \underbrace{f\times\bar{u}}_{COR} = \underbrace{\frac{-1}{\rho_w}\nabla p}_{PG} + \underbrace{\frac{\tau_s}{\rho_w D}}_{SSTR} + \underbrace{\frac{-\tau_b}{\rho_w D}}_{BSTR} + \underbrace{\nu\nabla^2\bar{u}}_{VISC} \qquad (3)$$

where $\bar{u}$ is the depth-averaged velocity (m/s), f is the Coriolis parameter (1/s), p is pressure (Pa), D is total depth (m), τ_s is surface stress (Pa), τ_b is bottom stress (Pa), and ν is kinematic viscosity (m^2/s). Here, the abbreviated terms are: ACC (local acceleration), ADV (horizontal advection), COR (Coriolis), PG (pressure gradient), SSTR (surface stress), BSTR (bottom stress), and VISC (horizontal viscosity). Note that the bold style letters represent vectors. The planar views of the momentum vectors reveal that the pressure gradient (PG), the surface stress (SSTR), and the bottom stress (BSTR) terms were primarily balanced when both normal and reverse surges were significant (Figs. 12–13). These results are generally consistent with those in Weisberg and Zheng (2006) and Zheng et al. (2013). We note that the residual terms (ACC, ADV, COR, and VISC in Figs. 12–13) seem to be smaller than those reported in the previous studies mentioned above. The reason can be attributed to the spatial variability in the momentum, as Chen et al. (2018) showed. For example, the horizontal advection term (ADV) can be locally larger at narrow channels; thus, the momentum balance in such locations may differ from the results shown in Fig. 12.

7. Discussions

Chen et al. (2018) and So et al. (2019) reported reverse surges along the coast of Florida inside Tampa Bay (the same location as this study)

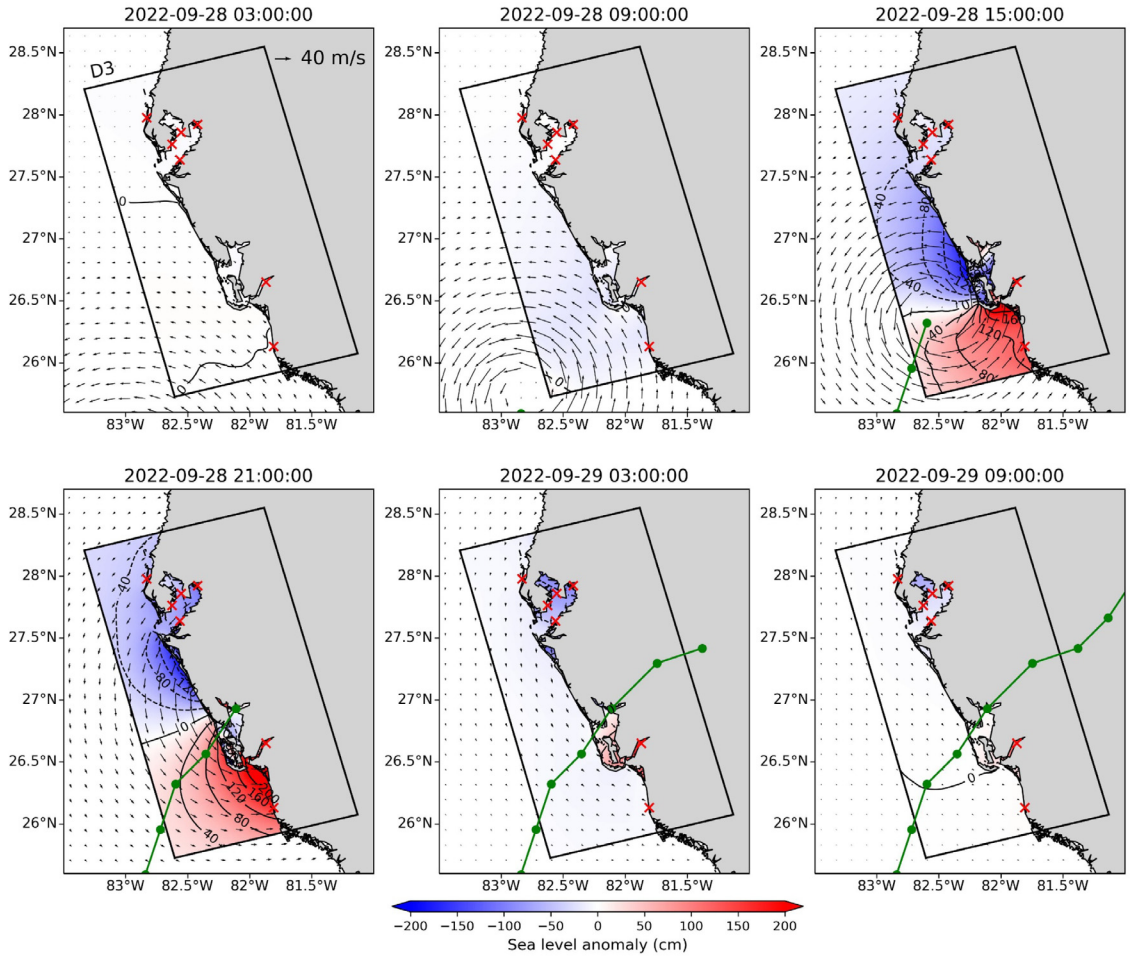

Fig. 11. Snapshots of simulated storm surge propagation at 6 h intervals during the September 2022 Hurricane Ian based on input data from the parametric typhoon model (PM). The location of the central position of Hurricane Ian is also shown (green line). The vectors represent the wind fields in the PM model.

during the 2017 Hurricane Irma. Returning to our research question on "what was the generation mechanism of reverse storm surges?", our investigations showed that the impact of seaward wind should dominate over that of pressure drop for reverse surge generation. However, this is not the case during many hurricanes and typhoons and therefore reverse surges are not always generated. For example, no reverse surges were reported during 2016 Typhoon Lionrock, 2017 Hurricane Maria, and 2018 Typhoon Jebi (Le et al., 2019; Heidarzadeh and Rabinovich, 2021; Heidarzadeh et al., 2018, 2021). To better illustrate the interactions of pressure drop and wind, we plotted their variations during Hurricane Ian in Fig. 14. Normal surges occurred precisely at those parts of the coast over which air pressure drop was the highest and strong landward winds were blowing simultaneously (Fig. 14). Reverse surges are observed at parts of the coast with noticeable air pressure drop, but less intense, and which simultaneously experienced seaward winds (Fig. 14). Despite the opposing effects of pressure drop and wind (i.e., negative air pressure increases sea level vs. seaward wind decreases it), reverse storm surges were larger (in absolute value) than normal surges. A detailed look at Fig. 14 reveals that this is at least partly because wind speed was smaller at tide gauges that experienced normal surges than at stations undergoing reverse surges. This might be due to: (i) spatial asymmetry of the hurricane's wind field, which can be seen both in measurements (Fig. 14), and in the HRRR (Fig. 8) and the ERA5 (Fig. 7) atmospheric models; and (ii) stations experiencing normal surges were closer to the calm hurricane eye.

The results of this study can be useful for coastal resilience and hazard awareness towards reverse storm surges. A primary hazard from reverse surges is the grounding of boats and ships due to the unexpected water level drop that can lead to some damage (e.g., Needham, 2022). Reverse surges can result in damage to port structures because the static water pressure is helpful for the stability of bulkheads and retaining walls within the ports and coastal areas. Such structures are normally designed assuming that static water pressure is always present seaward. Therefore, it is essential to re-design or strengthen such structures in case there is the risk of reverse storm surges in a coastal site. In addition, it is likely that some coastal residents start exploring the exposed seafloor during reverse surges which could make some health and safety issues for them from muddy grounds. Some ecological problems are also expected from exposed seafloor due to reverse storm surges (e.g., Corte et al., 2017). Although the hazards associated with normal surges are relatively well understood and appropriate mitigation plans are developed (such as protection to coastal flooding), reverse storm surges are mostly unknown to coastal communities, and therefore, coastal communities are unprotected against the hazards from reverse surges. We recommend that potential hazards from reverse storm surges be studied for coastal sites at risk, and appropriate warnings and mitigation plans be communicated to coastal communities.

As for limitations of this study, we note that the storm surge simulations were performed and evaluated using atmospheric forcings from two independent models, PM and HRRR, through two independent simulations. While our approach was successful in modelling the storm surges generated by Hurricane Ian, a hybrid PM-HRRR modelling could be an alternative approach (e.g., Liu and Sasaki, 2019). Other limitations of this study are attributed to the qualities of bathymetric data and the atmospheric models. We used the GEBCO_2022 bathymetric database for our simulations, which is thought to be of limited

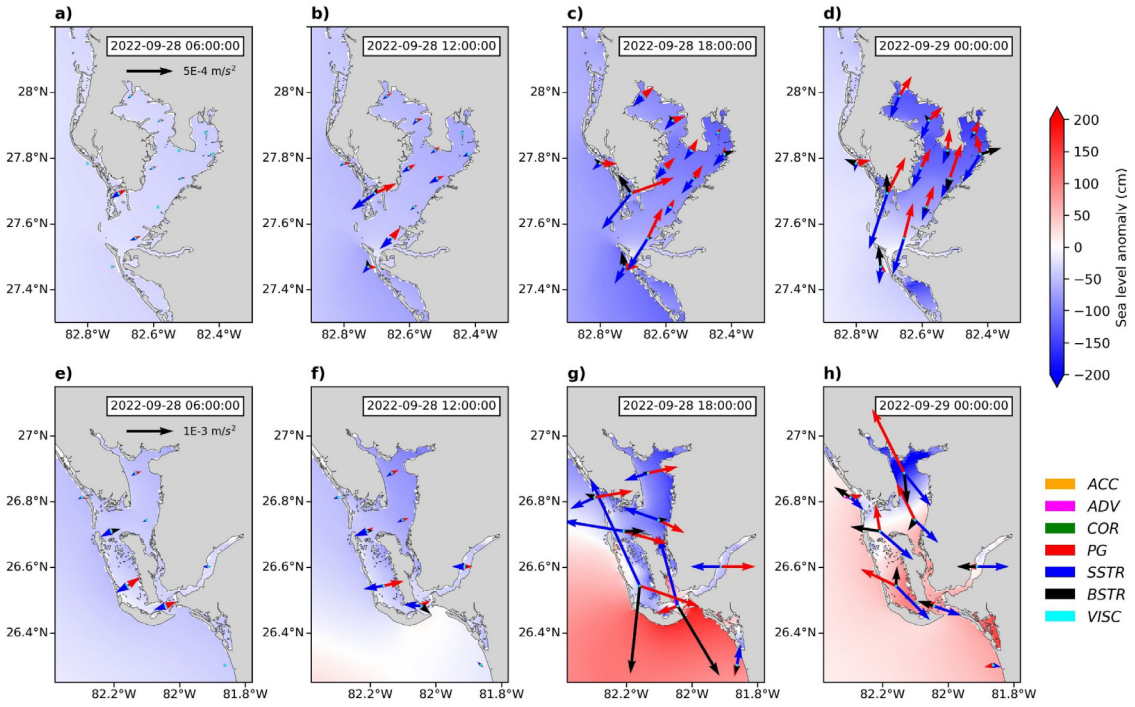

Fig. 12. **(a)** to **(d)** Same as Fig. 10 but around Tampa Bay. The vectors represent the barotropic momentums in Eq. (3) on the specific grid points. **(e)** to **(h)** Same as **a–d** but around Florida Keys, where the significant positive surge was observed. Abbreviations are: ACC (local acceleration), ADV (horizontal advection), COR (Coriolis), PG (pressure gradient), SSTR (surface stress), BSTR (bottom stress), VISC (horizontal viscosity).

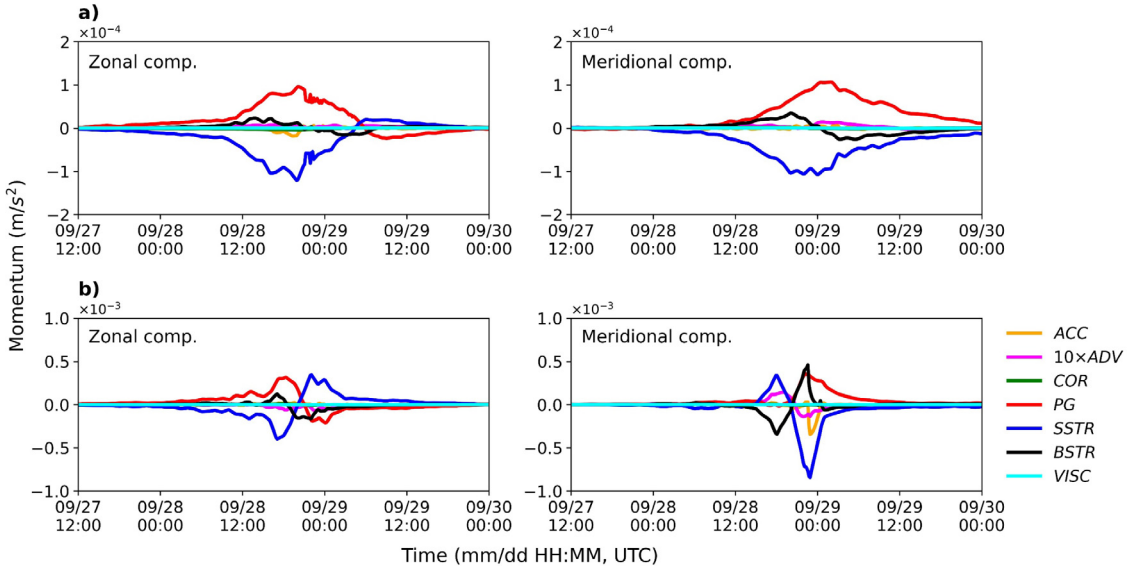

Fig. 13. **(a)** Time series of the zonal and meridional barotropic momentums given by Eq. (3) around the Tampa Bay. These time series are averaged values within the specific grid points. The values of ADV are multiplied by 10 in order to make them visible. **(b)** Same as (a) but around the Florida Keys. Abbreviations are: ACC (local acceleration), ADV (horizontal advection), COR (Coriolis), PG (pressure gradient), SSTR (surface stress), BSTR (bottom stress), VISC (horizontal viscosity).

accuracy in coastal areas; therefore, higher-resolution bathymetric data for coastal areas could further improve the simulations. The current atmospheric models are unable to address all changes during the evolution of a hurricane and thus it is expected that they might pose as a limitation of this study.

8. Conclusions

Coastal hazards from negative (reverse) storms surges during hurricanes and typhoons are less reported and understood although they can cause damage to coastal assets. The September 2022 Hurricane Ian was a rare event as it produced both positive (normal) and negative storm surges and thus provided the opportunity to study the generation mechanism of such rare coastal phenomenon. As no study was conducted on the generation mechanism of reverse storm surges, we performed this research to address the generation mechanism of reverse surges for the first time. Here, we employed a combination of sea level, air pressure, and wind velocity observations and developed a numerical model which is validated using observations. Our holistic study, employing a rich observation dataset of various types as well as modelling, enabled us to explain the generation mechanism of simultaneous occurrence of both normal and reverse surges for the first time. Main findings are:

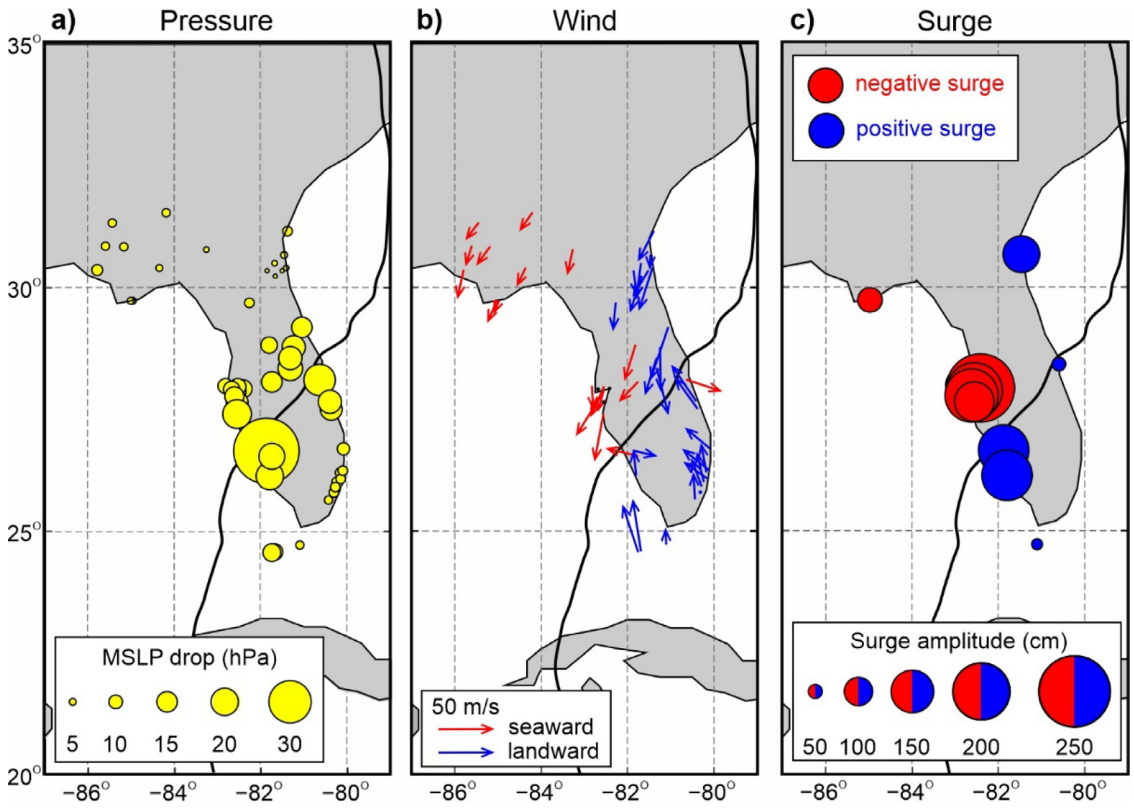

Fig. 14. The September 2022 Hurricane Ian over Florida, USA. Distribution of: **(a)** Maximum mean sea level pressure drop; **(b)** Wind velocity; and **(c)** Surge amplitude. In the middle panel, red arrows stand for seaward, and blue arrows for landward wind. In the right panel, red colour shows negative surge, and blue colour indicates positive surge. Black thick lines mark the track of the 2022 Hurricane Ian.

- Among the 11 tide gauge stations examined in this study, five of them produced normal surges where the maximum normal surge amplitudes varied from 0.4 m to over 1.8 m. Reverse surges were observed in six stations with maximum negative amplitudes of 0.9 m–2.4 m. This data reveals that reverse surges were larger than the normal ones.
- Analysis of air pressure data revealed that the maximum air pressure drop was 50 hPa observed in Fort Myers, approximately at the location of Ian's landfall, where air pressure reached a minimum value of 961.6 hPa. Maximum wind speed of 50–60 m/s was recorded during this event.
- Analysis of wind data reveals that all cases of normal and reverse surges during Hurricane Ian were consistently generated by landward and seaward winds, respectively, indicating that wind played a dominant role for the generation of storm surges over the pressure drop.
- Reverse surges occurred mostly at parts of the coast experiencing seaward wind and less intensive air pressure drop. Although pressure drop and wind have opposing impacts on the reverse surge generation (i.e., negative air pressure increases sea level whereas seaward wind decreases it), reverse storm surges were of larger amplitudes than normal surges, which further confirms that wind was the dominating factor for storm surge generation during hurricane Ian.
- Numerical simulations using two independent input models, the parametric model (PM) and the High-Resolution Rapid Refresh model (HRRR), showed that both simulations were successful in reproduction of the patterns of the storm surges. The PM model appeared to be more successful in reproducing normal surges, and the HRRR model performed better in reproducing reverse surges.
- Calculations of the momentum vectors through numerical modelling revealed that the pressure gradient, the surface stress, and the bottom stress terms were primarily balanced when both the normal and reverse surges were significant.
- Due to various hazards associated with reverse storm surges and lack of preparedness and mitigation plans for them in most coastal sites, our validated numerical model can be employed for forecasting reverse storm surges and designing mitigation strategies.

Availability of data and materials

Tide gauge data are available at the Tides & Currents NOAA (National Oceanic and Atmospheric Administration of the United States) portal (https://tidesandcurrents.noaa.gov/). Air pressure data can be downloaded at the ASOS (the Automated Surface Observing System) network (https://mesonet.agron.iastate.edu/request/asos/1min.phtml#). ERA5 data (global climate reanalysis data) are available at: https://cds.climate.copernicus.eu/cdsapp#!/home.

CRediT authorship contribution statement

Mohammad Heidarzadeh: Developed the idea, Conducted waveform analysis, Prepared the initial draft. **Takumu Iwamoto:** Performed numerical modelling, Wrote the relevant chapter. **Jadranka Šepić:** Conducted air pressure data analysis, Prepared the relevant text. **Iyan E. Mulia:** Prepared input data for the numerical model, Associated text.

Declaration of competing interest

The authors declare that they have no known competing financial interests or personal relationships that could have appeared to influence the work reported in this paper.

Data availability

Part of data used in this study are given in the body of the article. Other data will be made available on request to the corresponding author.

Acknowledgements

We are sincerely grateful to staff at the Tides & Currents NOAA (National Oceanic and Atmospheric Administration of the United States) portal and the ASOS (the Automated Surface Observing System) network for maintaining and providing the data used in this study. In particular, we acknowledge the great efforts by the NOAA scientist, Stuart Weinstein, for preparing the tide gauge data of this study. A number of figures were drafted using the GMT software (Wessel and Smith, 1998). The authors are grateful to the Associate Editor (Professor Yusuke Uchiyama) and two anonymous reviewers for their constructive review comments. All co-authors have read the final manuscript and commented on it.

Funding

We acknowledge University of Bath Institutional Open Access Fund, UK. Work of Jadranka Šepić was supported by the ERC-StG-853045 SHExtreme and the Croatian Science Foundation IP-2019-04-5875 StVar-Adri projects.

References

Benjamin, S.G., James, E.P., Brown, J.M., Szoke, E.J., Kenyon, J.S., Ahmadov, R., Turner, D.D., 2021. Diagnostic Fields Developed for Hourly Updated NOAA Weather Models. NOAA Technical Memorandum OAR GSL-66, http://dx.doi.org/10.25923/f7b4-rx42.

Benjamin, S.G., Weygandt, S.S., Brown, J.M., Hu, M., Alexander, C.R., Smirnova, T.G., Olson, J.B., James, E.P., Dowell, D.C., Grell, G.A., Lin, H., Peckham, S.E., Smith, T.L., Moninger, W.R., Kenyon, J.S., Manikin, G.S., 2016. A North American hourly assimilation and model forecast cycle: The rapid refresh. Mon. Weather Rev. 144 (4), 1669–1694. http://dx.doi.org/10.1175/MWR-D-15-0242.1.

Beven, J.L., Hagen, A., Berg, R., 2022. Tropical cyclone report: Hurricane ida (PDF) (report). Available at: https://www.nhc.noaa.gov/data/tcr/AL092021_Ida.pdf (Retrieved on 2nd October 2022).

Chen, J., Weisberg, R.H., Liu, Y., Zheng, L., 2018. The tampa bay coastal ocean model performance for Hurricane Irma. Mar. Technol. Soc. J. 52 (3), 33. http://dx.doi.org/10.4031/MTSJ.52.3.6.

Copernicus Climate Change Service (C3S), 2017. ERA5: Fifth generation of ECMWF atmospheric reanalyses of the global climate. Copernicus climate change service climate data store (CDS). date of access: 1 March 2023. https://cds.climate.copernicus.eu/cdsapp#!/home.

Corte, G.N., Schlacher, T.A., Checon, H.H., Barboza, C.A., Siegle, E., Coleman, R.A., Amaral, A.C.Z., 2017. Storm effects on intertidal invertebrates: increased beta diversity of few individuals and species. PeerJ 5, e3360. http://dx.doi.org/10.7717/peerj.3360.

Emanuel, K., 2003. Tropical cyclones. Annu. Rev. Earth Planet. Sci. 31, 75–104. http://dx.doi.org/10.1146/annurev.earth.31.100901.141259.

Fritz, H.M., Blount, C., Sokoloski, R., Singleton, J., Fuggle, A., McAdoo, B.G., Moore, A., Grass, C., Tate, B., 2007. Hurricane katrina storm surge distribution and field observations on the Mississippi Barrier islands. Estuar. Coast. Shelf Sci. 74 (1–2), 12–20. http://dx.doi.org/10.1016/j.ecss.2007.03.015.

Grinsted, A., 2008. Tidal fitting toolbox. https://uk.mathworks.com/matlabcentral/fileexchange/19099-tidal-fitting-toolbox. (Accessed 1 January 2023).

Heidarzadeh, M., Bonneton, P., Bonneton, N., Tissier, M., 2009. Field observations of wave-induced set-up on the French aquitanian coast. In: International Conference on Offshore Mechanics and Arctic Engineering, Vol. 43444. pp. 233–241.

Heidarzadeh, M., Gusman, A., Ishibe, T., Sabeti, R., Šepić, J., 2022. Estimating the eruption-induced water displacement source of the 15 january 2022 Tonga volcanic tsunami from tsunami spectra and numerical modelling. Ocean Eng. 261, 112165. http://dx.doi.org/10.1016/j.oceaneng.2022.112165%20.

Heidarzadeh, M., Harada, T., Satake, K., Ishibe, T., Takagawa, T., 2017. Tsunamis from strike-slip earthquakes in the Wharton basin, northeast Indian ocean: 2016 Mw 7.8 event and its relationship with the 2012 Mw 8.6 event. Geophys. J. Int. 47 (3), 1601–1612. http://dx.doi.org/10.1093/gji/ggx395.

Heidarzadeh, M., Iwamoto, T., Takagawa, T., Takagi, H., 2021. Field surveys and numerical modeling of the 2016 typhoon lionrock along the northeastern coast of Japan: The first typhoon making landfall in tohoku region. Nat. Hazards 105, 1–19. http://dx.doi.org/10.1007/s11069-020-04112-7.

Heidarzadeh, M., Rabinovich, A.B., 2021. Combined hazard of typhoon-generated meteorological tsunamis and storm surges along the coast of Japan. Nat. Hazards 106, 1639–1672. http://dx.doi.org/10.1007/s11069-020-04448-0.

Heidarzadeh, M., Teeuw, R., Day, S., Solana, C., 2018. Storm wave runups and sea level variations for the 2017 Hurricane Maria along the coast of Dominica, eastern Caribbean sea: evidence from field surveys and sea level data analysis. Coast. Eng. J. 60 (3), 371–384. http://dx.doi.org/10.1080/21664250.2018.1546269.

Hersbach, H., Bell, B., Berrisford, P., et al., 2020. The ERA5 global reanalysis. Q. J. R. Meteorol. 146, 1999–2049. http://dx.doi.org/10.1002/qj.3803.

Holland, G.J., 1980. An analytic model of the wind and pressure profiles in hurricanes. Mon. Weather Rev. 108, 1212–1218. http://dx.doi.org/10.1175/1520-0493(1980)108%3c1212:AAMOTW%3e2.0.CO;2.

Jones, J.E., Davies, A.M., 2004. Influence of wind field and open boundary input upon computed negative surges in the Irish sea. Cont. Shelf Res. 24 (17), 2045–2064. http://dx.doi.org/10.1016/j.csr.2004.07.002.

Kimball, S.K., Mulekar, M.S., 2004. A 15-year climatology of north Atlantic tropical cyclones. Part I: Size parameters. J. Clim. 3555–3575. http://dx.doi.org/10.1175/1520-0442(2004)017%3c3555:AYCONA%3e2.0.CO;2.

Knapp, K.R., Diamond, H.J., Kossin, J.P., Kruk, M.C., Schreck, C.J., 2018. International best track archive for climate stewardship (IBTrACS) project, version 4. http://dx.doi.org/10.25921/82TY-9E16.

Knapp, K.R., Kruk, M.C., Levinson, D.H., Diamond, H.J., Neumann, C.J., 2010. The international best track archive for climate stewardship (IBTrACS): Unifying tropical cyclone data. Bull. Am. Meteorol. Soc. 91, 363–376. http://dx.doi.org/10.1175/2009BAMS2755.1.

Landsea, C.W., 1993. A climatology of intense (or major) Atlantic hurricanes. Mon. Wea. Rev. 121 (6), 1703–1713. http://dx.doi.org/10.1175/1520-0493(1993)121%3c1703:ACOIMA%3e2.0.CO;2.

Le, T.A., Takagi, H., Heidarzadeh, M., Takata, Y., Takahashi, A., 2019. Field surveys and numerical simulation of the 2018 typhoon jebi: Impact of high waves and storm surge in semi-enclosed Osaka bay, Japan. Pure Appl. Geophys. 176 (10), 4139–4160. http://dx.doi.org/10.1007/s00024-019-02295-0.

Liu, F., Sasaki, J., 2019. Hybrid methods combining atmospheric reanalysis data and a parametric typhoon model to hindcast storm surges in Tokyo bay. Sci. Rep. 9, 12222. http://dx.doi.org/10.1038/s41598-019-48728-7.

Merrill, R.T., 1984. A comparison of large and small tropical cyclones. Mon. Wea. Rev. 112, 1408–1418. http://dx.doi.org/10.1175/1520-0493(1984)112%3c1408:ACOLAS%3e2.0.CO;2.

Mitsuyasu, H., Honda, T., 1982. Wind-induced growth of water waves. J. Fluid Mech. 123, 425–442. http://dx.doi.org/10.1017/S0022112082003139.

Mulia, I.E., Ueda, N., Miyoshi, T., Iwamoto, T., Heidarzadeh, M., 2023. A novel deep learning approach for typhoon-induced storm surge modeling through efficient emulation of wind and pressure fields. Sci. Rep. 13, 7918. http://dx.doi.org/10.1038/s41598-023-35093-9.

Musinguzi, A., Akbar, M.K., 2021. Effect of varying wind intensity, forward speed, and surface pressure on storm surges of Hurricane Rita. J. Mar. Sci. Eng. 9 (2), 128.

Nakamura, R., Mäll, M., Shibayama, T., 2019. Street-scale storm surge load impact assessment using fine-resolution numerical modelling: a case study from Nemuro. Japan. Nat. Hazards 99 (1), 391–422. http://dx.doi.org/10.1007/s11069-019-03746-6.

Needham, H., 2022. The science behind negative storm surges – field report from hurricane ian. Available at: https://www.geo-trek.com/posts/the-science-behind-negative-storm-surges-field-report-from-hurricane-ian#:~:text=If%20the%20hurricane%20is%20approaching,a%20sudden%2C%20negative%20storm%20surge. (Accessed on 26th June 2023).

NHC (National Hurricane Centre), 2018. Costliest U.S. Tropical Cyclones Tables Update. United States National Hurricane Center, Available at: https://www.nhc.noaa.gov/news/UpdatedCostliest.pdf (Retrieved on 2nd October 2022).

NHC (National Hurricane Centre), 2022. Five-day graphical tropical weather outlook. Available at: https://www.nhc.noaa.gov/archive/xgtwo/gtwo_archive.php?current_issuance=202209192102&basin=atl&fdays=5 (Retrieved on 2nd October 2022).

NOAA (National Centers for Environmental Information), 2022. Monthly national climate report for 2022. https://www.ncei.noaa.gov/access/monitoring/monthly-report/national/202209/supplemental/page-5 (accessed 29 March 2023).

Peng, M., Xie, L., Pietrafesa, L.J., 2006. Tropical cyclone induced asymmetry of sea level surge and fall and its presentation in a storm surge model with parametric wind fields. Ocean Model. 14 (1–2), 81–101. http://dx.doi.org/10.1016/j.ocemod.2006.03.004.

Rahman, M.A., Zhang, Y., Lu, L., et al., 2022. Relative accuracy of HWRF reanalysis and a parametric wind model during the landfall of hurricane florence and the impacts on storm surge simulations. Nat. Hazards http://dx.doi.org/10.1007/s11069-022-05702-3.

Rego, J.L., Li, C., 2010. Nonlinear terms in storm surge predictions: Effect of tide and shelf geometry with case study from Hurricane Rita. J. Geophys. Res. 115 (C6).

Sebastian, T., Lendering, K., Kothuis, B., Brand, N., Jonkman, B., van Gelder, P., Godfroij, M., Kolen, B., Comes, T., Lhermitte, S., Meesters, K., van de Walle, B., Ebrahimi Fard, A., Cunningham, S., Khakzad, N., Nespeca, V., 2017. Hurricane Harvey Report: A Fact-Finding Effort in the Direct Aftermath of Hurricane Harvey in the Greater Houston Region. Delft University Publishers, p. 103, Available at: https://pure.tudelft.nl/ws/portalfiles/portal/31283193/TU_Delft_Texas_Hurricane_Harvey_Report_Phase_I_20171108.pdf.

Shchepetkin, A.F., McWilliams, J.C., 2005. The regional oceanic modeling system (roms): a split-explicit, free-surface, topography-following-coordinate oceanic model. Ocean Modell. 9 (4), 347–404. http://dx.doi.org/10.1016/j.ocemod.2004.08.002.

Slocum, C.J., Razin, M.N., Knaff, J.A., Stow, J.P., 2022. Does ERA5 mark a new era for resolving the tropical cyclone environment?. J. Clim. 35, 3457–3564. http://dx.doi.org/10.1175/JCLI-D-22-0127.1.

So, S., Juarez, B., Valle-Levinson, A., Gillin, M.E., 2019. Storm surge from hurricane irma along the florida peninsula. Estuar. Coast. Shelf Sci. 229, 106402.

Toyoda, M., Fukui, N., Miyashita, T., Shimura, T., Mori, N., 2022. Uncertainty of storm surge forecast using integrated atmospheric and storm surge model: a case study on typhoon haishen 2020. Coast. Eng. J. 64, 135–150. http://dx.doi.org/10.1080/21664250.2021.1997506.

Wang, Y., Su, H.Y., Ren, Z., Ma, Y., 2022. Source properties and resonance characteristics of the tsunami generated by the 2021 m 8.2 alaska earthquake. J. Geophys. Res. Oceans 127 (3), e2021JC018308. http://dx.doi.org/10.1029/2021JC018308.

Weatherall, P., Marks, K.M., Jakobsson, M., Schmitt, T., Tani, S., Arndt, J.E., Rovere, M., et al., 2015. A new digital bathymetric model of the world's oceans. Earth Space Sci. 2 (8), 331–345. http://dx.doi.org/10.1002/2015EA000107.

Weisberg, R.H., Zheng, L., 2006. Hurricane storm surge simulations for tampa bay. Estuar. Coasts: J. Estuar. Res. Fed 29 (6), 899–913. http://dx.doi.org/10.1007/BF02798649.

Wessel, P., Smith, W.H.F, 1998. New improved version of generic mapping tools released. EOS Trans Am Geophys Union 79 (47), 579–579.

WMO (World Meteorological Organization), 2011. Guide To Storm Surge Forecasting. WMO-No. 1076, p. 120, Available online at: https://library.wmo.int/doc_num.php?explnum_id=7747 (accessed on 21st January 2023).

Zheng, L., Weisberg, R.H., Huang, Y., Luettich, R.A., Westerink, J.J., Kerr, P.C., Donahue, A.S., Crane, G., Akli, L., 2013. J. Geophys. Res. C: Oceans 118 (7), 3350–3369. http://dx.doi.org/10.1002/jgrc.20248.